energy&fuels

pubs.acs.org/EF Article

Analysis of Sequential Adsorption−Oxidation of VOCs on Atomic Layer-Deposited PtNi/ZrO_2−SiO_2 Dual-Function Materials

Busuyi O. Adebayo, Han Yu, Ali A. Rownaghi, Xinhua Liang, and Fateme Rezaei*

Cite This: https://doi.org/10.1021/acs.energyfuels.2c01013 Read Online

ACCESS | Metrics & More | Article Recommendations | Supporting Information

ABSTRACT: To develop efficient dual-function materials (DFMs) for capture and destruction of volatile organic compounds (VOCs), we prepared a series of composite materials comprising PtNi nanoparticles supported on ZrO_2-promoted SiO_2 (PtNi/ZrO_2−SiO_2) via atomic layer deposition (ALD) method and investigated them for sequential adsorption and desorption/catalytic oxidation of benzene, as a model VOC compound. ZrO_2 was first deposited on a unimodal SiO_2 support, followed by deposition of Pt and Ni nanoparticles with varried amount. Dynamic adsorption experiments were conducted using a 500 ppm_v-laden feed at 25 °C and 1 atm, followed by in situ catalytic oxidation at 200 °C. Among the DFMs investigated, 1Pt2Ni/ZrSi emerged as the material with overall in situ conversion of ∼96% due to its retaively high PtNi acid sites density compared with other DFMs. Kinetic analysis was conducted on 1Pt2Ni/ZrSi by investigating the effects of feed concentration, regenerative feed flow rate, and oxidation temperature on the benzene conversion in the sequential adsorption−oxidation process. The results of the kinetic analysis revealed that a complete oxidation can be attained over 1Pt2Ni/ZrSi and its performance can be improved upon decreasing adsorptive feed benzene concentration (maximum value of 99.7% at 125 ppm_v) and regenerative feed flow rate (100% at 5 mL/min), and increasing oxidation temperature (100% at 200 °C). Overall, the obtained results highlighted the optimal operation conditions for sequential adsorption and oxidation of VOCs over ALD-based DFMs.

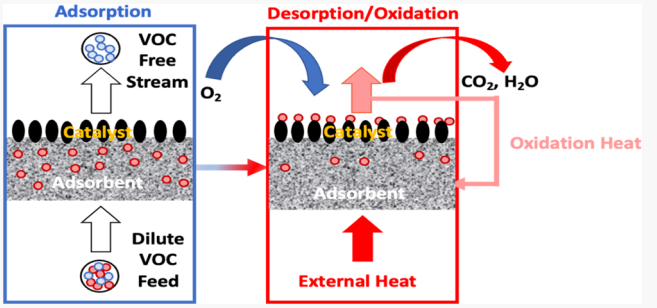

1. INTRODUCTION

Human carcinogens, majorly benzene, toluene, and xylene (BTX), are among the most common volatile organic compounds (VOCs).[1] Thermal and catalytic combustion, as well as adsorption, have traditionally been used to remove these chemicals from air or process streams; however, other approaches such as absorption and biofiltration have also been tried.[2,3] Various cutting edge advancements have been made toward effective VOC control, no doubt, but yet a lot still needs to be done as environmental regulations continue to be more stringent. Adsorption is a prominent method for controlling VOCs; nevertheless, its effectiveness diminishes when low to ultralow concentrated streams are involved and likewise when the VOC source is humid. Thermal oxidation on the other hand is extremely energy-intensive, while catalytic oxidation, the supposedly alternative to thermal oxidation for energy reduction, requires a large inventory of expensive catalysts. Furthermore, catalytic oxidation also suffers from various deactivation processes, such as fouling/coking, poisoning, and aging/sintering. As a result of all of these and even more, research is still ongoing to develop better approaches for effective and efficient VOC abatement under diverse conditions.

Integrated abatement techniques such as adsorptive reactors, are being studied to solve the disadvantages of the existing thermal/catalytic incineration or adsorption technologies. To ensure process intensification including a reduction in capital investment, catalyst inventory, or any need for external heating or cooling, the use of adsorptive reactors has become an emerging technology. Hybrid adsorption and catalytic oxidation can either be simultaneous or sequential. In the sequential method, which is the focus of this work, a dilute stream of VOCs is first concentrated via adsorption, followed by catalytic oxidation, in which the previously adsorbed VOCs are oxidized to less harmless compounds, predominantly H_2O and CO_2. Oxidation of the adsorbed VOCs can either be in situ (oxidation directly in the adsorbed state) desorption followed by oxidation, or their combination. In a proof-of-concept work by Kullavanijaya et al.,[4] the integrated adsorption reaction technique was used to adsorb VOC from its stream, after which the adsorbed VOC was thermally or catalytically combusted to innocuous H_2O and CO_2. Later, the same group[5] first adsorbed binary VOC mixtures on activated carbon

Received: April 4, 2022
Revised: June 2, 2022

and then combusted the captured VOCs on $Pd/CeO_2/Al_2O_3$ catalysts. In a similar work by Nikolajsen et al.,[6] sintered-metal-fiber-supported bifunctional adsorbent-catalyst materials were investigated for sequential adsorption and oxidation of a dilute VOC-laden air stream. Their results revealed an excellent efficacy of the investigated materials and methods. Through employing bifunctional Ru/HZSM-5 materials, Wang et al.[7] utilized this same hybrid method to remove bulky aromatic compounds of toluene, *o*-xylene, and 1,3,5-trimethylbenzene from their streams. Via numerical modeling and simulation, Kolade et al.[8] investigated the feasibility of the use of sequential adsorptive reactive technology for the abatement of VOCs. In our recent publication on the subject matter, numerical parametric analysis was carried out on a Ni/ZrO_2-SiO_2 dual-function material (DFM) to assess the effects of the process operating conditions on the performance of the DFMs.[9]

More recently, we embarked on development of a series of DFMs as viable candidates for the abatement of dilute streams of VOCs in a hybrid process. The first group of materials investigated was mixed-metal oxides (MMOs) consisting of TiO_2 and ZrO_2 coated on SiO_2. The materials, co-synthesized via the sol−gel method, resulted in toluene overall in situ conversion of 86% (TiO_2-SiO_2) and 71% (ZrO_2-SiO_2) at the selected operating conditions.[10] With the aim of utilizing the high adsorption capability of a metal−organic framework (MOF) material, we, next, investigated TiO_2/MIL-101(Cr) and Pd/MIL-101(Cr) composites. The TiO_2 or Pd was wet-impregnated on the MIL-101(Cr). While TiO_2/MIL-101(Cr) showed toluene conversion of 88%, Pd/MIL-101(Cr) exhibitted a conversion of only 80%, the difference being attributed to the small size of the TiO_2/MIL-101(Cr) particles.[11] Not satisfied with the performance of these materials, we investigated another group of DFMs prepared by atomic layer deposition (ALD) of metal oxide followed by noble metal(s) on our SiO_2 support. First, in this group, the ZrO_2 film was deposited on SiO_2, followed by the deposition of Ni nanoparticles by ALD (Ni/ZrO_2-SiO_2). The materials displayed acceptable surface properties with benzene overall in situ conversion of 85−96% depending on the Ni loading.[12] Moreover, platinum has been reported by many authors as an excellent catalyst for combustion of VOCs. In our most recent publication,[13] Pt/TiO_2 or Pt/ZrO_2 on SiO_2 DFMs was investigated for combined adsorption and catalytic destruction of benzene. Pt/ZrO_2-SiO_2 outperformed its Pt/TiO_2-SiO_2 counterpart with benzene overall conversion efficiency of ∼100%. Unfortunately, because Pt is a precious metal, the choice of Pt as a catalyst in this investigation is not viable. To balance high abatement efficiency with process capital and operating costs, the choice of bimetallic PtNi is now being considered. In the current study, kinetic analysis is conducted to investigate the effects of adsorptive feed VOC concentration, regenerative feed flow rate, and oxidation temperature on the performance of PtNi/ZrSi for sequential adsorption-catalytic oxidation of benzene. Similar kinetic analysis, but via numerical parametric analysis, carried out on the Ni/ZrO_2-SiO_2 DFM was reported in our recent publication.[9] This is the first extensive study of the experimental investigation of the effects of the process operating conditions on the performance of an integrated sequential adsorption-catalytic abatement of VOCs.

2. EXPERIMENTAL SECTION

2.1. Materials. All the chemicals and gases used in this work were used as purchased, with no further purification. Helium (ultrahigh purity), hydrogen, nitrogen, and oxygen gases were purchased from Airgas. The following chemicals used in this work were purchased from Sigma-Aldrich: triethanolamine (TEAH, $(HOCH_2CH_2)_3N$, 98% purity), tetraethyl orthosilicate (TEOS, $Si(OC_2H_5)_4$, 99% purity), hexadecyltrimethylammonium bromide (CTAB, $CH_3(CH_2)_{15}N(Br)-(CH_3)_3$), electronic grade tetrakis(dimethylamido)zirconium(IV) ($Zr-(NMe_2)_4$ of purity ≥ 99.99%), and electronic grade bis-(cyclopentadienyl)nickel(II) ($Ni(cp)_2$, $Ni(C_5H_5)_2$ of purity ≥ 99.98%). Electronic grade (methylcyclopentadienyl)trimethyl platinum(IV) ($(MeCp)PtMe_3$, $C_5H_4CH_3Pt(CH_3)_3$ of purity ≥ 99.98%) was purchased from Strem.

2.2. Material Synthesis. In our previous paper,[14] the synthesis of the UVM-7 silica support used in this work was described in detail. Similarly, the details of the ALD's home-built fluidized bed reactor used in this work are detailed elsewhere.[15] Briefly, ZrO_2 was first deposited on the UVM-7 silica support using the ALD method. Similarly, the ALD was used to deposit highly dispersed Pt and Ni nanoparticles on top of the ZrO_2 coating. Before the beginning of ALD, the porous silica was outgassed under vacuum for 3 h at 200 °C. Five cycles of ZrO_2 ALD were administered on the bare SiO_2 support. Typically, one cycle of ZrO_2 ALD started with a $Zr(NMe_2)_4$ dose, a N_2 flush, deionized water dose, and finally, another N_2 dose as a flush. During a ZrO_2 ALD cycle, $Zr(NMe_2)_4$ was delivered into the reactor after being heated to 80 °C as the reactor was heated up and sustained at 200 °C. Pt and Ni ALD shared the same procedure. Similarly, a typical Pt ALD cycle included a $(MeCp)PtMe_3$ dose and then a N_2 flush, followed by an O_2 dose, and finally, a N_2 flush. After heating the reactor to 100 °C, $(MeCp)PtMe_3$ was injected into it, and the process was maintained at 300 °C. Pt and Ni nanoparticles should sit together and form a "twinned" structure, but not an alloy or core−shell structure, similar to Pt−Co nanoparticles that were prepared by ALD.[16] The final synthesized DFMs were named *x*Pt*y*Ni/ZrSi where *x* and *y* are the number of ALD cycles of Pt and Ni deposited on the ZrO_2-SiO_2 composite, respectively.

2.3. Material Characterization. High-angle powder X-ray diffraction (XRD) spanning 5−90° was conducted on the materials to assess their crystallinity using a PANalytical X'Pert multifunctional X-ray diffractometer of Cu Kα radiation (λ_1 = 1.5406, λ_2 = 1.5444 and Kα_2/Kα_1 = 1/2) and a 2θ = 0.7°/min scan rate. In this experiment, SIL'TRONIX zero diffraction silicon plates were utilized to eliminate any background noise from the measurements. To reveal the interior surface morphology of the samples, transmission electron microscopy (TEM) was conducted on each sample on a Zeiss Merlin Gemini field emission microscope (FE-SEM). N_2 physisorption experiments were conducted at −196 °C to assess the textural properties of the materials using a Micromeritics 3Flex surface characterization analyzer. For each experiment, 0.1 g of the material of interest was loaded in a tube, fitted on a Micromeritics Smart VacPrep, and then degassed under vacuum for 12 h at 250 °C. The surface areas of the materials were estimated in the relative pressure range of $0.05 < P/P^{sat} < 0.35$ using the linearized Brunauer−Emmett−Teller (BET) model, while pore size distribution (PSD) was determined using the density functional theory (DFT) cylindrical geometry classical N_2-Hasley model . A field emission scanning electron microscope (Zeiss Merlin Gemini) was used to perform transmission electron microscopy (TEM) on the materials to access their morphology. Additionally, to calculate the surface elemental compositions and the chemical states of the materials, X-ray photoelectron spectroscopy (XPS) analysis (aluminum being the X-ray source) was conducted on a Kratos Axis 165 photoelectron spectrometer. The surface acidity of the materials was also investigated by temperature-programmed desorption of ammonia (NH_3-TPD) in a U-shaped quartz reactor (8 mm I.D.). The material of interest (0.1 g) was loaded in the reactor, degassed for 1 h at 400 °C under a He flow, cooled to 80 °C under the same He flow, exposed to a 5% NH_3/He flow at 30 mL/min for 30 min, and then exposed to a He flow to remove physisorbed NH_3. Finally, the temperature was increased from 80 to 800 °C at a ramp rate of 10 °C/min for NH_3 desorption to take place under a He flow.

2.4. Benzene Adsorption Experiments. Equilibrium adsorption experiments were conducted via isotherm measurements to probe the feasibility of the materials for potential separation/purification applications. Benzene vapor equilibrium adsorption isotherms were

https://doi.org/10.1021/acs.energyfuels.2c01013
Energy Fuels XXXX, XXX, XXX−XXX

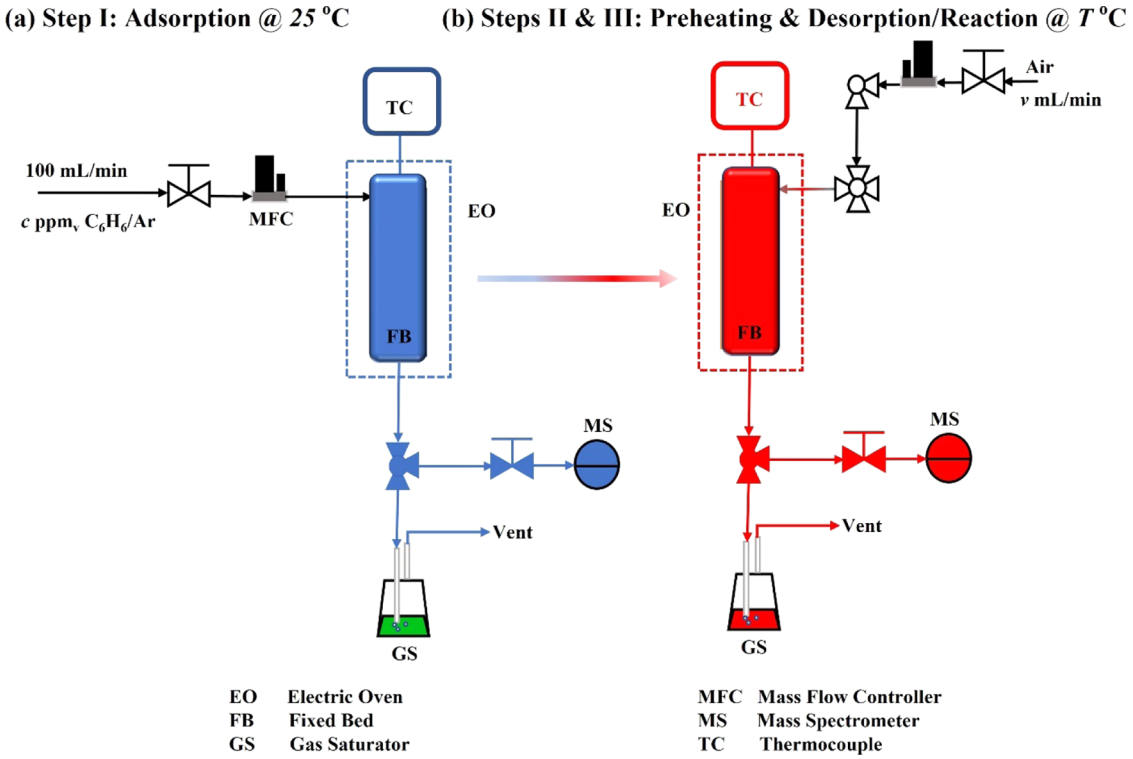

Figure 1. Single-column sequential adsorption and desorption/catalytic oxidation experiment schematic for (a) adsorption and (b) preheating and desorption/catalytic oxidation steps.

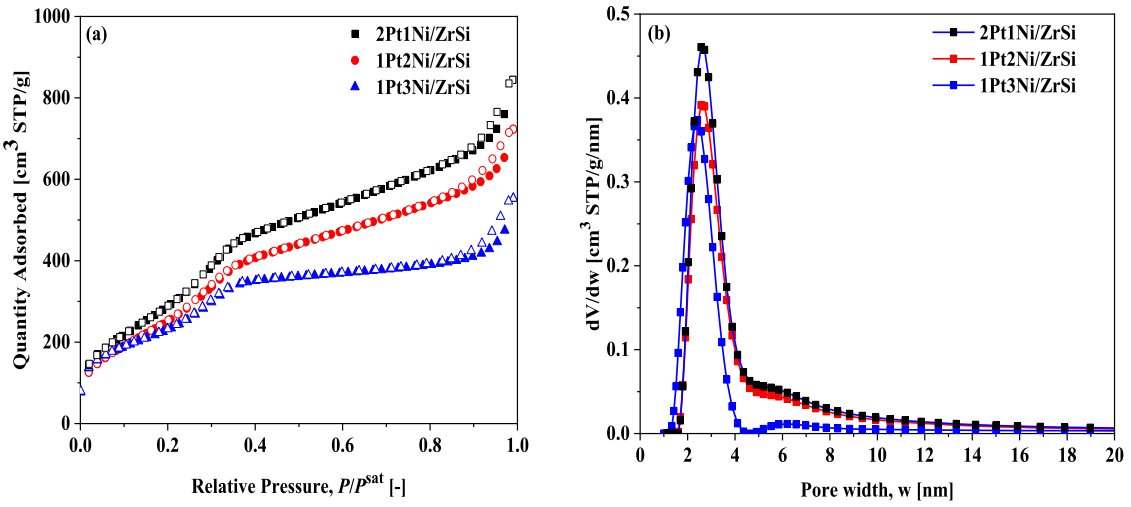

Figure 2. (a) N_2 physisorption isotherms and (b) PSD profiles of the DFMs.

collected at 25 °C on the Micromeritics 3Flex surface characterization analyzer. The benzene vapor was generated at 25 °C and 1 atm from a liquid benzene reservoir and kept in a water bath at 25 °C, using the repeated freeze thaw mechanism. These measurementes were carried out by loading 0.1 g of the material of interest in a capped BET tube and then degassing for 6 h at 250 °C followed by cooling to 25 °C. Finally, the BET tube, with its degassed sample, was transferred to the Micromeritics 3Flex for isotherm measurements.

For dynamic adsorption, breakthrough experiments were conducted in a 304 stainless-steel column reactor (bed dimension: height = 0.02 m, radius = 0.005 m) at ~1 atm and 25 °C. Gas flow rates were controlled by Brooks mass flow controllers, whereas the temperature was controlled by a combination of heating tape, K-type thermocouple, and Omega bench controller. In the experiments, 0.2 g of the material of interest was packed in the columnand then degassed at 250 °C under a 40 mL/min Ar flow for an hour. The bed was then cooled to the adsorption temperature (25 °C) and the system was allowed to stabilize at that temperature for about 30 min. Thereafter, adsorption was initiated by a continuous flow of 100 mL/min benzene/Ar stream to the inlet of the bed, while the bed outlet concentration was monitored and collected on-line using a BELMass mass spectrometer. The equations used to calculate dynamic adsorption capacities are presented in the Supporting Information.

2.5. Sequential Adsorption and Desorption/Catalytic Oxidation Experiments. The catalytic oxidation step was started immediately after a 5% breakthrough, i.e., $p_{out,Benzene}/p_{in,Benzene} = 0.05$; adsorption was attained at the adsorptive feed conditions same as used for dynamic adsorption experiments but with varying adsorptive feed VOC concentration, c ppm_v. After the attainment of 5% breakthrough adsorption, the process and its setup (Figure 1) were switched from the adsorption step to preheating (very brief, less than 2 min) and the

https://doi.org/10.1021/acs.energyfuels.2c01013
Energy Fuels XXXX, XXX, XXX−XXX

desorption/catalytic oxidation step. The brief external preheating part in this step was to heat up the bed from the adsorption temperature to the desorption temperature (~100 °C) and then to the variable catalytic oxidation temperature of T °C after which the external heat source was removed to harness the released exothermic heat of reaction for autothermal operation. During this step, regenerative airflow of v mL/min was continuously supplied to the bed inlet and its outlet concentrations were monitored and collected on-line using the BELMass mass spectrometer, while any potential carbon monoxide formation was also collected on-line using Enerac 700 connected to a computer. The equations used to calculate overall benzene conversions are discussed in the Supporting Information.

3. RESULTS AND DISCUSSIONS

3.1. Material Characterization. The N_2 physisorption isotherms and the PSD profiles of the ALD-based DFMs are depicted in Figure 2. The N_2 physisorption isotherms (Figure 2a) all displayed similar shapes, suggesting that the pore structure of the materials is similar. These isotherms were all of the type IV classification according to the IUPAC isotherm classification.[17] The first N_2 physisorption occurred in $P/P^{sat} \leq 0.2$, the second in $0.2 \leq P/P^{sat} \leq 0.4$, and the last in $P/P^{sat} > 0.4$. The equilibrium adsorption could be associated with capillary condensation of N_2 taking place within the mesopores of the materials.[18] Moreover, the materials showed type H1 hysteresis in their isotherms, indicating the presence of relatively large cylindrical pores within the porous network structure of the materials.[19] The maximum N_2 uptakes took the order of 2Pt1Ni/ZrSi (850 cm^3/g) > 1Pt2Ni/ZrSi (725 cm^3/g) > 1Pt3Ni/ZrSi (550 cm^3/g). It should also be noted here that all the investigated DFMs displayed reduced N_2 uptake relevant to the bare SiO_2, as expected, due to the pore blockage after deposition of ZrO_2 and the Pt/Ni nanoparticles. From the PSD profiles shown in Figure 2b, it is notable that all of the materials possessed two distinct pore sizes with peaks centered at about 2.5 and 6.5 nm. The PSD profiles were also found to be relatively similar in shape, implying similar pore structures for the studied DFMs.

The textural properties of the materials estimated from the N_2 physisorption isotherms are summarized in Table 1. The specific surface area and total pore volume decreased in the order of 2Pt1Ni/ZrSi (1341 m^2/g and 1.13 cm^3/g) > 1Pt2Ni/ZrSi (1162 m^2/g and 0.97 cm^3/g) > 1Pt3Ni/ZrSi (980 m^2/g and 0.90 cm^3/g). An increase in the Ni nanoparticles loading appeared to reduce the surface area and porosity of the DFMs, whereas Pt deposition did not alter the textural properties significantly. The bare silica's total surface area and pore volume were also estimated to be 1376 m^2/g and 1.13 cm^3/g, respectively. Pt1Ni/ZrSi possessed the highest micropore volume at 0.17 cm^3/g, followed by 1Pt3Ni/ZrSi at 0.11 cm^3/g and then 1Pt2Ni/ZrSi at 0.05 cm^3/g. The mesopore volumes however took a different trend: 2Pt1Ni/ZrSi still exhibited the highest at 0.96 cm^3/g, followed by 1Pt2Ni/ZrSi at 0.92 cm^3/g and then 1Pt3Ni/ZrSi at 0.59 cm^3/g. Moreover, while the average pore diameters of 2Pt1Ni/ZrSi and 1Pt2Ni/ZrSi were identical, at 2.6 and 5.2 nm, those of 1Pt3Ni/ZrSi were estimated to be 2.4 and 6.1 nm.

Table 1. Textural Properties of the DFMs Estimated from N_2 Physisorption Isotherms

	BET surface area	pore volume			pore diameter
sample	[m^2/g]	micropore [cm^3/g]	mesopore [cm^3/g]	total [cm^3/g]	[nm]
bare SiO_2	1376	0.19	0.86	1.17	3.0, 5.2
2Pt1Ni/ZrSi	1341	0.17	0.96	1.13	2.6, 5.2
1Pt2Ni/ZrSi	1162	0.05	0.92	0.97	2.6, 5.2
1Pt3Ni/ZrSi	980	0.11	0.59	0.70	2.4, 6.1

The TEM images in Figure 3 reveal that the size of DFM nanoparticles (PtNi/ZrSi) fell in the range of 25−50 nm. Moreover, given the small size and low loading of the Pt and Ni NPs that were deposited on the ZrO_2−SiO_2 support, they were essentially indistinguishable, and the shape could not be clearly seen in the figures, but the Pt and Ni NPs deposited by the ALD method have been shown to be generally less than 2 nm and about 3−4 nm in size, respectively.[20] Another observation from these images is the uniform deposition of metal nanoparticles on the MMO support, highlighting the suitability of the ALD method to prepare these DFMs.

XPS analysis was performed to quantify the surface elemental compositions and oxidation states of the metals in the DFMs. The profiles are illustrated in Figure 4. All of the spectra were adjusted with the adventurous C 1s peak observed at 284.5 eV. For nickel, Ni $2p_{3/2}$ together with its satellite counterpart was detected around 855.6 and 861 eV, respectively, while Ni $2p_{1/2}$ together with its satellite counterpart was detected around 873 and 880 eV, respectively (Figure 4a). As it is well known, the satellite peaks stem from the shake-up electrons.[21] The splitting between Ni $2p_{1/2}$ and Ni $2p_{3/2}$ peaks of Ni^{2+} was estimated to be 18.4 eV, in accordance with the literature reports. Surface nickel of the materials occurred in the form Ni^{2+} either from NiO and/or from $Ni(OH)_2$, based on the work of Biesinger et al.[22] The oxygen O 1s characteristic peak was detected at 533 eV (Figure 4b), while the silicon Si 2p characteristic peak was observed in all of the materials at a binding energy location of 103.5 eV, which was attributed to Si in SiO_2 (Figure 4c). Figure 4d reveals that platinum was detected as Pt 4f at 76.2 (Pt $4f_{5/2}$) and 72.5 (Pt $4f_{7/2}$) eV. In Figure 4e, two zirconium Zr 3d characteristic peaks were detected in all of the materials: Zr $3d_{3/2}$ at 184 eV and $3d_{5/2}$ at 182 eV, corresponding with Zr^{4+}. However, as revealed in Figure 4e and in Table 2, it should be noted that there was a slight difference in the ZrO_2 content of the materials even though the same number (here 5) of ZrO_2 ALD cycles was administered on all of them. This slight difference was not unexpected though, due to machine measurement error. The Si, Zr, and O XPS spectra were in agreement with the observation reported in previous work.[12,13] The intensities of all of the peaks gradually decreased with Ni loading, which was due to the coverage of the ZrO_2−SiO_2 surface by the Ni phase at higher Ni loading.[22]

The surface elemental compositions of the materials extracted from XPS spectra are listed in Table 2. First, O and Si in the materials were in the range of 65.23−65.97% and 32.78−33.19%, respectively, which indicated uniformity in the O and Si compositions across all of the DFMs. A higher oxygen content is usually desirable to facilitate the catalytic activity of the DFMs, however, the XPS results revealed no significant changes in the oxygen content across the ALD-based samples. As expected, the Pt atomic wt % loading on 2Pt1Ni/ZrSi was about twice on the other two samples. However, the Ni amount was slightly changed between the three ALD cycles. The Ni amount on 2Pt3Ni/ZrSi was slightly higher than the amounts on 1Pt2Ni/ZrSi and 2Pt1Ni/ZrSi. The total bimetallic atomic wt % increased from 2Pt1Ni/ZrSi (1.07%) to 1Pt3Ni/ZrSi (0.90%) and 1Pt2Ni/ZrSi (0.87%). The atomic weight percents of Zr on

https://doi.org/10.1021/acs.energyfuels.2c01013
Energy Fuels XXXX, XXX, XXX−XXX

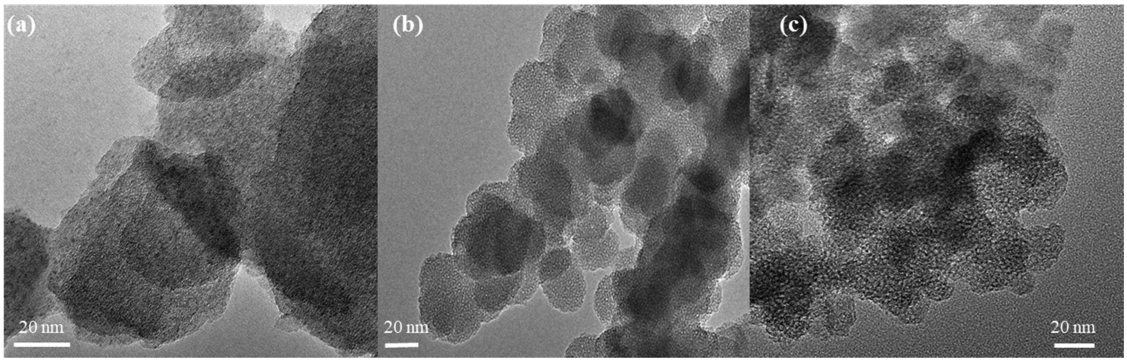

Figure 3. TEM images of (a) 2Pt1Ni/ZrSi, (b) 1Pt2Ni/ZrSi, and (c) 1Pt3Ni/ZrSi samples.

the surface of the materials were 0.42−0.53%, which is similar to expected.

High-angle XRD patterns of the ALD-based DFMs are shown in Figure 5a. First, the silica characteristic diffraction peak commonly found around $2\theta = 22-23°$ and indexed as the plane (101) was detected in all of the materials.[23,24] However, the broadness of this peak indicates that the materials lack any long-range orderly arrangement of atoms. A comparison of these diffraction patterns revealed that Pt and Ni nanoparticles' deposition on the composite ZrO_2-SiO_2 support had no significant effect on the degree of crystallinity of the support. This suggests that the ZrO_2 deposition resulted in ultrathin ZrO_2 or amorphous, small, and well-dispersed ZrO_2 particles, or that the Pt and Ni nanoparticles were small and well-dispersed on the support.[25,26] Another plausible explanation could be the relatively low content of the metal NPs in these materials, which did not cause any observable changes to the crystalline structure of the MMO.

In addition to the crystallinity of the DFMs, their surface acidity was also investigated using NH_3-TPD; the results of which are presented in Figure 5b. Physisorption/weak acid sites typically occurred in the low-temperature region of less than 200 °C, whereas moderate and strong acid sites occured in the temperature domains of 200−500 °C and > 500 °C, respectively. Clearly, one major asymmetrical peak was observed in each sample in the range of 100−400 °C, indicating the presence of weak−moderate acid sites on their surfaces. The peak areas and intensities followed the trend: 1Pt2Ni/ZrSi > 1Pt3Ni/ZrSi ≈ 2Pt1Ni/ZrSi. Shown in Table 3 are the total acid site concentration and density of the materials. Clearly, while the concentration of acid sites on the materials followed the order: 2Pt1Ni/ZrSi (0.3024 mmol NH_3/g) > 1Pt3Ni/ZrSi (0.2770 mmol NH_3/g) > 1Pt2Ni/ZrSi (0.2327 mmol NH_3/g), the acid site density took 1Pt2Ni/ZrSi (7.69×10^{-5} mmol NH_3/m^2) > 1Pt3Ni/ZrSi (5.48×10^{-5} mmol NH_3/m^2) > 2Pt1Ni/ZrSi (3.72×10^{-5} mmol NH_3/m^2).

3.2. Benzene Adsorption Properties. Adsorption isotherms of benzene vapor are shown in Figure 6a. According to the IUPAC classification, we can see that all of the materials depicted the type IV isotherm, which depicts three sequential steps of adsorption: monolayer and multilayer adsorption, and capillary condensation.[17] Going across the materials, the end of the monolayer adsorption occurred around $P/P^{sat} < 0.15$, while the end of the multilayer adsorption occurred around $P/P^{sa} > 0.20$. In between these two steps was the multilayer adsorption step. In the low partial pressure region, the equilibrium uptake of benzene over the three materials was remarkably similar; however, as partial pressure increased, 2Pt1Ni/ZrSi outperformed its two counterparts showing 13% higher uptake than 1Pt2Ni/ZrSi and 26% than 1Pt3Ni/ZrSi, with capacities being 6.30, 5.59, and 5.01 mmol/g, respectively, at $P/P^{sat} = 0.5$. The trend in the VOC uptake seen here can be linked to their specific surface area, as shown in Table 1, in that the material with the higest surface area displayed the highest benzene vapor uptake. In our previous work,[12] we reported benzene adsorption capacities of 1.52, 1.25, and 1.08 mmol/g at $P/P^{sat} = 0.5$ for 1Ni/ZrSi, 2Ni/ZrSi, and 3Ni/ZrSi, respectively; however, it should be noted that the ZrO_2-SiO_2 supports in that work possessed much lower surface area and micropore volume (due to the bimodal nature of SiO_2) than those reported in this work (i.e., with unimodal SiO_2 support). It was also observed that with the increase in Ni loading, the benzene adsorption decreased progressively, primarily due to the reduction in surface area with increasing Ni loading, as discussed earlier; however, with respect to Pt nanoparticles, no general trend could be observed.

To gain a better understanding of the dynamic adsorption of benzene over this series of ALD-based DFMs, the breakthrough experiments were performed, and the corresponding concentration fronts are illustrated in Figure 6b. Key parameters calculated from the breakthrough profiles are presented in Table 4. The blank run was included therein to show the hydrodynamics of benzene in the empty column. At first glance, the trends observed herein could be linked to the textural and surface qualities of the materials as well as to the bed porosity andweight, and inlet conditions.[27] However, as the dynamic experiments were investigated at the same inlet conditions and bed weight with similar bed porosity, it was conclusive that material properties are the dominant factors of the characteristic times. Moreover, it is conclusive that the equilibrium adsorption uptakes and the dynamic adsorption uptakes and characteristic times are all explainable based on the same rationale. From dynamic point of view, the breakthrough times (i.e., $t_{0.05}$) for 2Pt1Ni/ZrSi and 1Pt2Ni/ZrSi were very close and about 2.5 times of that for 1Pt3Ni/ZrSi, whereas in the case of saturation times (i.e., $t_{1.0}$) this difference reduced to only ∼1.1 times. It should also be noted here that the q_{eq} values obtained here are much smaller than those reported in our earlier work,[12] due to much lower VOC inlet concentration (∼500 vs ∼85000 ppm_v).

3.3. Sequential Adsorption−Oxidation Performances. The results of the sequential adsorption−oxidation experiments are illustrated in Figure 7. The spikes shown in Figure 7a represent the thermal runaways of the desorbed C_6H_6 from the materials that had not been reacted and consequently left the bed.[12] Notably, benzene concentration decreased shortly after thermal runaway attained its maximum level. This was due to the fact that gaseous holdup of benzene at the end of adsorption had

https://doi.org/10.1021/acs.energyfuels.2c01013
Energy Fuels XXXX, XXX, XXX−XXX

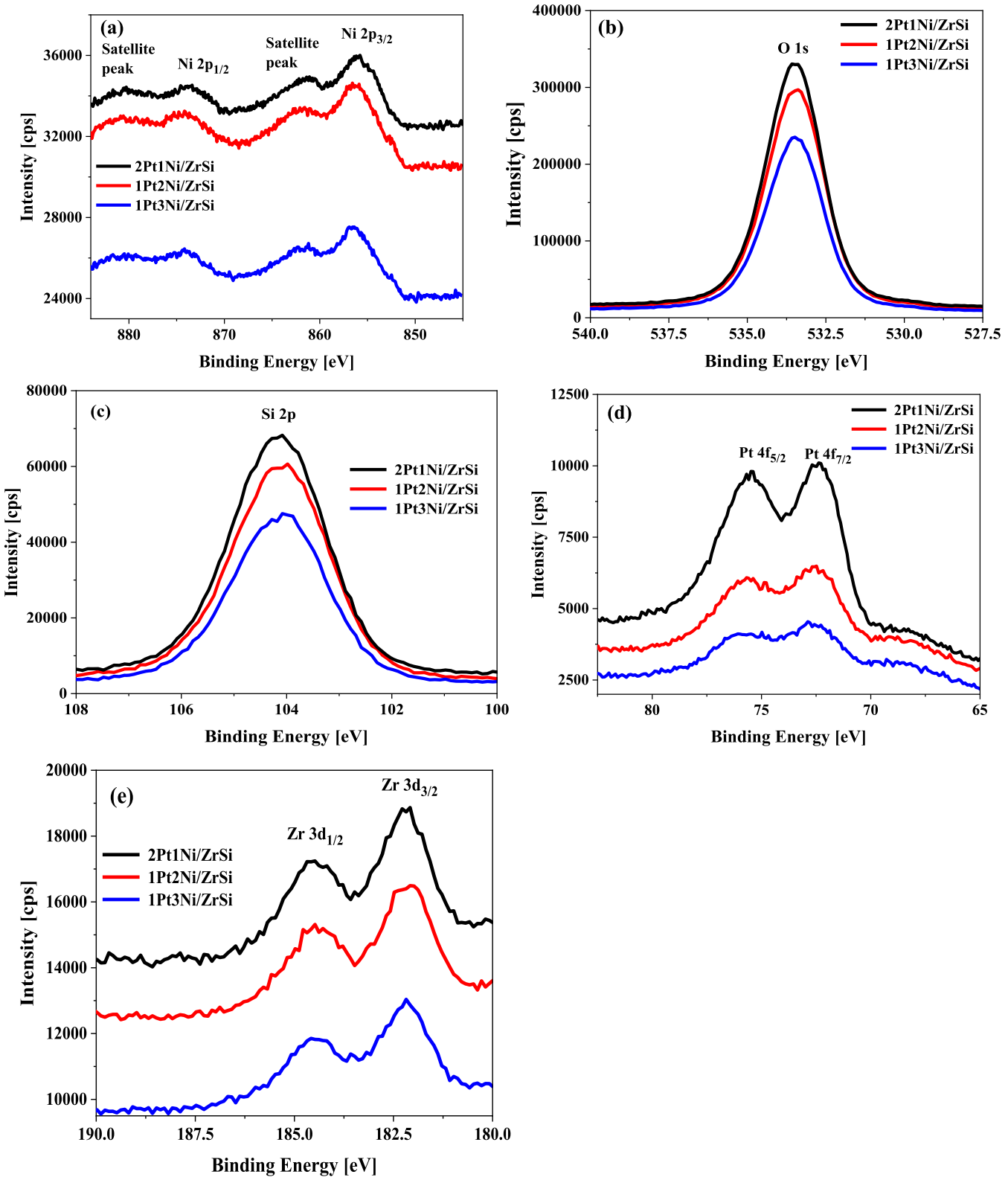

Figure 4. High-resolution XPS spectra for (a) nickel, (b) oxygen, (c) silicon, (d) platinum, and (e) zirconium of the DFMs.

exited the bed or on the other hand reacted, while the rate of desorption was higher than that of oxidation. Thus, it is conclusive that the excess of desorption over oxidation was the detected benzene profile. Moreover, the desorption/catalytic oxidation kinetics were very fast as revealed by the sharp and narrow profile of the benzene thermal runaways, which could be linked to the decrease in pore diameter with increased adsorption, thereby creating a barrier to fast diffusion of desorbed benzene within the pores, and consequently increasing the rate of oxidation.[18] Figure 7**b** shows the CO_2 evolution during the reaction, while Figure 7c shows the H_2O counterpart.

https://doi.org/10.1021/acs.energyfuels.2c01013
Energy Fuels XXXX, XXX, XXX−XXX

Table 2. Atomic Weight Percent Surface Elemental Compositions of the Materials via XPS

sample	Ni atomic [wt %]	O atomic [wt %]	Pt atomic [wt %]	PtNi[a] atomic [wt %]	Si atomic [wt %]	Zr atomic [wt %]
2Pt1Ni/ZrSi	0.57	65.23	0.50	1.07	33.16	0.46
1Pt2Ni/ZrSi	0.56	65.20	0.32	0.87	33.39	0.53
1Pt3Ni/ZrSi	0.64	65.97	0.26	0.90	32.78	0.42

[a]PtNi loading = Pt loading + Ni loading.

Table 3. Acid Site Quantification of the Materials Estimated from NH_3-TPD

sample	PtNi total acid sites concentration [mmol NH_3/g]	PtNi total acid sites density[a] [mmol NH_3/m^2]
2Pt1Ni/ZrSi	0.3024	3.72×10^{-5}
1Pt2Ni/ZrSi	0.2327	7.69×10^{-5}
1Pt3Ni/ZrSi	0.2770	5.48×10^{-5}

[a]Total acid site density = Total acid site concentration/BET surface area.

Overall desorption/catalytic oxidation performance of the materials is summarized in Table 5. Because there was no CO formation, the key performance indicator used to assess the performance of the DFMs in this process was benzene overall conversion. As shown, the benzene overall in situ conversion was highest for 1Pt2Ni/ZrSi at 96.1%, followed by 1Pt3Ni/ZrSi at 94.3%, and then 2Pt1Ni/ZrSi at 91.5%. It should be noted that there was no correlation between the amount adsorbed, the runaway amount adsorbed, and the overall in situ conversion. However, the trend observed herein is directly proportional to the acid sites density trend depicted in Table 3. Given a similar surface oxygen content for these three DFMs, it is plausble to assume that the difference in acid sites density is the main factor contributing to the different catalytic behaviours. Although the thermal runaway of 1Pt3Ni/ZrSi was the lowest at 0.003 mmol/g, the dynamic amount adsorbed was equivalently low, as similarly reported by Wang et al.[28] Moreover, for 2 cycles of ALD-deposited Ni on ZrO_2−SiO_2 (i.e., 2Ni/ZrSi), a conversion of 92% was reported for benzene in our earlier work,[12] albeit with a different inlet feed concentration (86100 ppm_v) than was used here.

3.4. Effect of Process Parameters on Benzene Overall Conversion. In this section, an in-depth analysis on the effect of process parameters such as feed concentration, regenerative feed flow rate, and oxidation temperature, controlling benzene overall conversion, was carried out using the best-performing DFM (1Pt2Ni/ZrSi). In the first case, the experiments were carried out using feeds of varied benzene concentrations (125, 250, and 500 ppm_v) while keeping other operating conditions constant, i.e., adsorptive feed flow rate, pressure, and temperature at 100 mL/min, 1 atm, and 25 °C, respectively; regenerative feed flow rate, pressure, and composition at 20 mL/min, 1 atm, and 21% O_2/79% N_2, respectively; and oxidation temperature at 200 °C. The results of the investigation are shown in Figure 8a. It is evident that the benzene overall conversion decreased with increasing adsorptive feed VOC concentrations: 99.7, 97.5, and 96.5% at 125, 250, and 500 ppm_v, respectively. This has been attributed to the higher loading at high VOC concentrations, thus decreasing the tendency for complete in situ oxidation of the desorbed C_6H_6.[8]

It is essential to assess the effect of feed flow rate during desorption/catalytic oxidation step on the overall catalytic activity of the DFM. In the second case, the regenerative feed flow rate was varied from 5 to 20 and 50 ppm_v to assess its impact on benzene overall conversion, while other factors were kept constant, i.e., adsorptive feed VOC concentration = 125 ppm_v, flow rate = 100 mL/min, pressure = 1 atm, and temperature = 25 °C; regenerative feed flow rate = 20 mL/min, pressure = 1 atm, composition = 21% O_2/79% N_2, and oxidation temperature = 250 °C. The results of the investigation are shown in Figure 8b. As apparent from this figure, the benzene overall conversion decreased with the increasing regenerative feed flow rate, this is mainly becuase at higher regenerative flow rates, the residence time of the regenerative oxidant feed decreases, which in turn reduces the conversion of the desorbed C_6H_6, as also demonstrated by Urbutis and Kitrys.[29]

Aiming at assessing the oxidation temperature on the overall abatement performance of our selected DFM, the oxidation temperature was varied from 150 to 200 and 250 °C, while other operating conditions were kept constant, i.e., adsorptive feed VOC concentration, flow rate, pressure, and temperature at 125 ppm_v, 100 mL/min, 1 atm, and 25 °C, respectively; regenerative

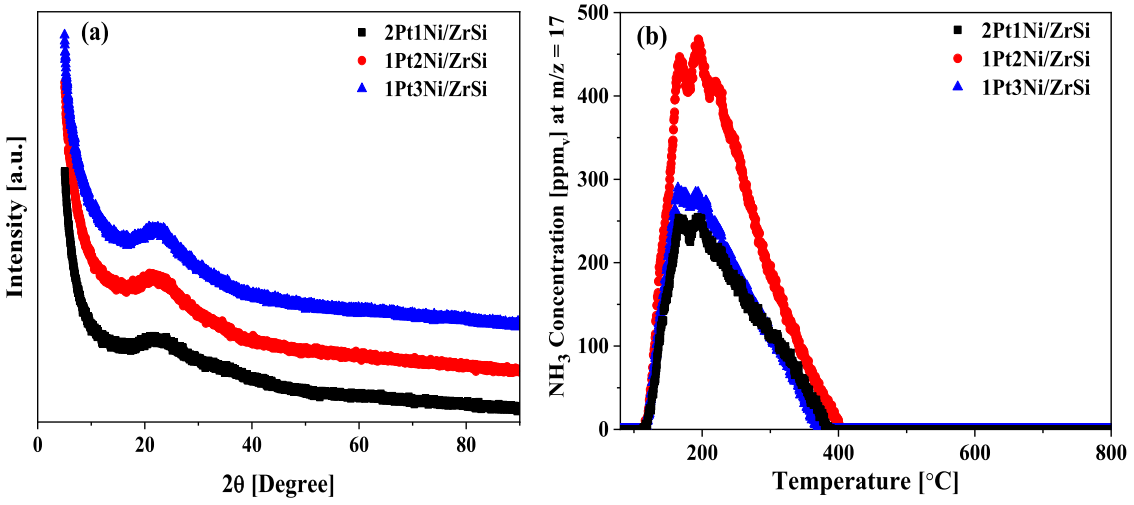

Figure 5. (a) High-angle XRD patterns and (b) NH_3-TPD profiles of the DFMs.

https://doi.org/10.1021/acs.energyfuels.2c01013
Energy Fuels XXXX, XXX, XXX−XXX

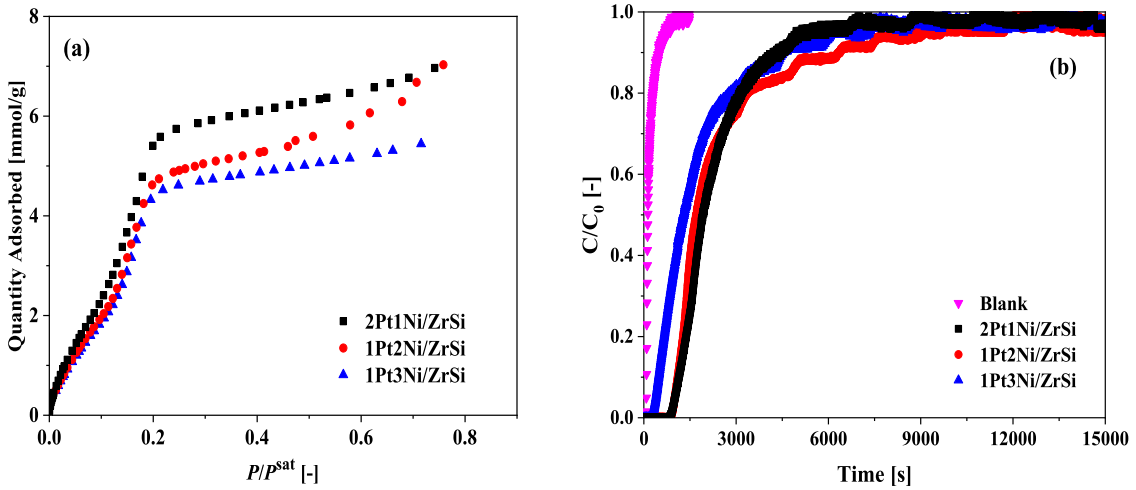

Figure 6. (a) Benzene vapor isotherms and (b) benzene breakthrough profiles; experimental conditions: bed initially saturated with Ar at 25 °C and 1 atm, 100 mL/min 500 ppm_v C_6H_6/Ar inlet feed at 25 °C and 1 atm.

Table 4. Material Dynamic Adsorption Data Obtained from Benzene Breakthrough Profiles

sample	$t_{0.05}$ [s]	$t_{1.0}$ [s]	$q_{d,0.05}$ [mmol/g]	$q_{d,1.0}$ [mmol/g]	q_{eq} [mmol/g]
2Pt1Ni/ZrSi	1006	10 050	0.16	1.47	1.48
1Pt2Ni/ZrSi	1001	10 002	0.15	1.46	1.47
1Pt3Ni/ZrSi	400	9200	0.06	1.33	1.33

Table 5. Benzene Oxidation Performance Variables (Runaway Amount and Overall Conversion)

sample	amount adsorbed [mmol/g]	runaway amount [mmol/g]	overall conversion [%]
2Pt1Ni/ZrSi	0.166	0.009	91.5
1Pt2Ni/ZrSi	0.157	0.006	96.1
1Pt3Ni/ZrSi	0.054	0.003	94.3

feed flow rate, pressure, and composition of 5 mL/min, 1 atm, and 21% O_2/79% N_2, respectively. The results of the investigation are shown in Figure 8c. For this effect, it was observed that over this material a complete oxidation can be achieved at temperatures as low as 200 °C, whereas the oxidation temperature of 150 °C can give rise to conversions >96%. It should be noted here that although it is possible to even achieve a complete VOC destruction at temperatures lower than 200 °C by increasing the amount of catalyst nanoparticles, the adsorption properties of the DFM may be compromised. Therefore, a judicious choice of process parameters should not only consider a balance between adsorption and desorption efficiencies but also should account for DFM composition and properties. Ultimately, the economics of the hybrid process would dictate the choice of both materials and operating conditions.

4. CONCLUSIONS

In this project, unimodal SiO_2 coated first with ultrathin ZrO_2 film was decorated with PtNi nanoparticles of varried loadings via the ALD method. The resulting DFMs were characterized and then first evaluated for adsorption of benzene at 25 °C and 1 atm. Sequential adsorption-oxidation in air was conducted at 125−500 ppm_v adsorptive feed VOC concentration, 5−50 mL/min regenerative feed flow rate, and 150−250 °C oxidation temperature. 1Pt2Ni/ZrSi displayed the best dual-functional capability with 96.1% abatement efficiency at adsorptive feed VOC concentration of 500 ppm_v, regenerative feed flow rate of 20 mL/min, and oxidation temperature of 200 °C, compared

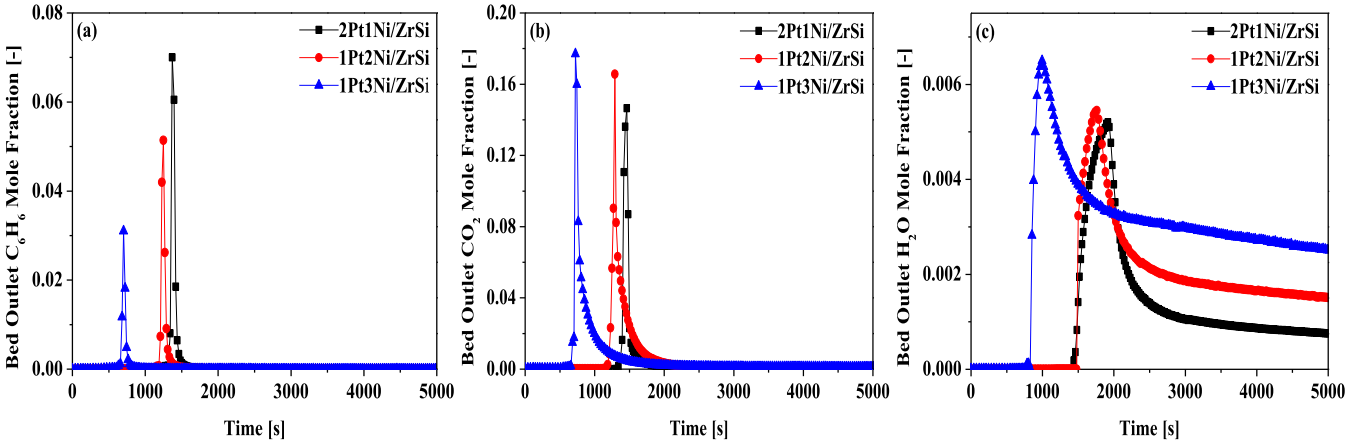

Figure 7. Adsorption-oxidation profiles for (a) C_6H_6 thermal runaway, (b) CO_2 evolution, and (c) H_2O evolution: adsorption till 5% breakthrough at 500 ppm_v C_6H_6/Ar feed at 25 °C, 1 atm and 100 mL/min, oxidation temperature = 200 °C, and regenerative feed flow rate = 20 mL/min.

https://doi.org/10.1021/acs.energyfuels.2c01013
Energy Fuels XXXX, XXX, XXX−XXX

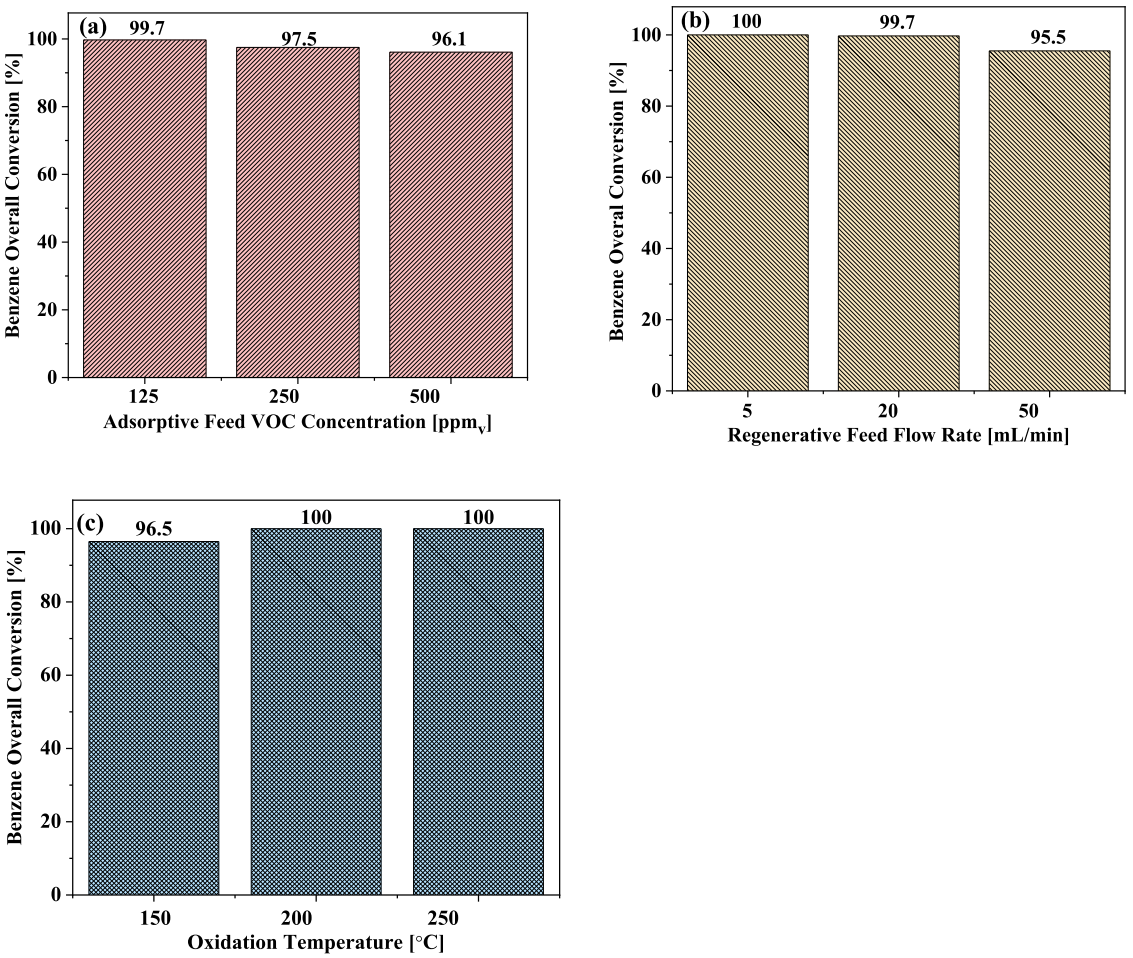

Figure 8. Effects of (a) adsorptive feed concentration, (b) regenerative feed flow rate, and (c) oxidation temperature on the overall benzene conversion in 1Pt2Ni/ZrSi DFM.

with 1Pt3Ni/ZrSi and 2Pt1Ni/ZrSi. The superior perfoamce of this material was correlated to its higher acid sites density than those of its two other counterparts. Further investigation by kinetic analysis revealed that the performance of the 1Pt2Ni/ZrSi can be enhanced by adjusting process conditions such as reducing adsorptive feed VOC concentration (maximum value of 99.7% at 125 ppm$_v$) and regenerative feed flow rate (100% at 5 mL/min), and increasing oxidation temperature (100% at 200 °C). Overall, the results of this investigation revealed that novel ALD-prepared PtNi/ZrSi materials all have the potential to be effective dual-function materials for abating dilute streams of VOCs, specifically aromatic hydrocarbons.

■ ASSOCIATED CONTENT

Supporting Information

The Supporting Information is available free of charge at https://pubs.acs.org/doi/10.1021/acs.energyfuels.2c01013.

Dynamic adsorption capacity calculations and *in situ* conversion estimations (PDF)

■ AUTHOR INFORMATION

Corresponding Author

Fateme Rezaei − *Department of Chemical & Biochemical Engineering, Missouri University of Science and Technology, Rolla, Missouri 65409, United States;* orcid.org/0000-0002-4214-4235; Email: rezaeif@mst.edu

Authors

Busuyi O. Adebayo − *Department of Chemical & Biochemical Engineering, Missouri University of Science and Technology, Rolla, Missouri 65409, United States*

Han Yu − *Department of Chemical & Biochemical Engineering, Missouri University of Science and Technology, Rolla, Missouri 65409, United States*

Ali A. Rownaghi − *Department of Chemical & Biochemical Engineering, Missouri University of Science and Technology, Rolla, Missouri 65409, United States;* orcid.org/0000-0001-5228-5624

Xinhua Liang − *Department of Chemical & Biochemical Engineering, Missouri University of Science and Technology, Rolla, Missouri 65409, United States;* orcid.org/0000-0001-7979-0532

Complete contact information is available at: https://pubs.acs.org/10.1021/acs.energyfuels.2c01013

Notes

The authors declare no competing financial interest.

■ ACKNOWLEDGMENTS

The authors thank the National Science Foundation (NSF CBET-1802049) for financially supporting this project.

https://doi.org/10.1021/acs.energyfuels.2c01013
Energy Fuels XXXX, XXX, XXX−XXX

REFERENCES

(1) Liaud, C.; Nguyen, N. T.; Nasreddine, R.; Le Calvé, S. Experimental Performances Study of a Transportable GC-PID and Two Thermo-Desorption Based Methods Coupled to FID and MS Detection to Assess BTEX Exposure at Sub-Ppb Level in Air. *Talanta* **2014**, *127*, 33−42.

(2) Gelles, T.; Krishnamurthy, A.; Adebayo, B.; Rownaghi, A.; Rezaei, F. Abatement of Gaseous Volatile Organic Compounds: A Material Perspective. *Catal. Today* **2020**, *350*, 3−18.

(3) Krishnamurthy, A.; Adebayo, B.; Gelles, T.; Rownaghi, A.; Rezaei, F. Abatement of Gaseous Volatile Organic Compounds: A Process Perspective. *Catal. Today* **2020**, *350*, 100−119.

(4) Kullavanijaya, E.; Trimm, D. L.; Cant, N. W. Adsocat: Adsorption/Catalytic Combustion for VOC and Odour Control. In *Studies in Surface Science and Catalysis*; Elsevier, 2000; Vol. *130*, pp 569−574.

(5) Kullavanijaya, E.; Cant, N. W.; Trimm, D. L. The Treatment of Binary VOC Mixtures by Adsorption and Oxidation Using Activated Carbon and a Palladium Catalyst. *J. Chem. Technol. Biotechnol.* **2002**, *77*, 473−480.

(6) Nikolajsen, K.; Kiwi-Minsker, L.; Renken, A. Structured Fixed-Bed Adsorber Based on Zeolite/Sintered Metal Fibre for Low Concentration VOC Removal. *Chem. Eng. Res. Des.* **2006**, *84*, 562−568.

(7) Wang, Y.; Yang, D.; Li, S.; Chen, M.; Guo, L.; Zhou, J. Ru/hierarchical HZSM-5 zeolite as efficient bi-functional adsorbent/catalyst for bulky aromatic VOCs elimination. *Microporous Mesoporous Mater.* **2018**, *258*, 17−25.

(8) Kolade, M. A.; Kogelbauer, A.; Alpay, E. Adsorptive Reactor Technology for VOC Abatement. *Chem. Eng. Sci.* **2009**, *64*, 1167−1177.

(9) Adebayo, B. O.; Rezaei, F. Modeling of Temperature Swing Adsorption-Oxidation of Volatile Organic Compounds. *Chem. Eng. Sci.* **2022**, *250*, No. 117356.

(10) Adebayo, B. O.; Krishnamurthy, A.; Rownaghi, A. A.; Rezaei, F. Toluene Abatement by Simultaneous Adsorption and Oxidation over Mixed-Metal Oxides. *Ind. Eng. Chem. Res.* **2020**, *59*, 13762−13772.

(11) Adebayo, B. O.; Krishnamurthy, A.; Al-Naddaf, Q.; Rownaghi, A. A.; Rezaei, F. Investigation of Combined Capture-Destruction of Toluene over Pd/MIL-101 and TiO_2/MIL-101 Dual Function Materials. *Energy Fuels* **2021**, *35*, 13256−13267.

(12) Adebayo, B. O.; Newport, K.; Yu, H.; Rownaghi, A. A.; Liang, X.; Rezaei, F. Atomic Layer Deposited Ni/ZrO2−SiO_2 for Combined Capture and Oxidation of VOCs. *ACS Appl. Mater. Interfaces* **2020**, *12*, 39318−39334.

(13) Adebayo, B. O.; Yu, H.; Rownaghi, A. A.; Liang, X.; Rezaei, F. Atomic Layer Deposited Pt/TiO_2−SiO_2 and Pt/ZrO_2−SiO_2 for Sequential Adsorption and Oxidation of VOCs. *Chem. Eng. J.* **2022**, *444*, No. 136603.

(14) Adebayo, B. O.; Lawson, S.; Rownaghi, A. A.; Rezaei, F. Analysis of Equilibrium and Dynamic Adsorption of Benzene Vapor over Unimodal and Bimodal Silica-Based Mixed-Metal Oxides. *Chem. Eng. J.* **2020**, *396*, No. 125273.

(15) Liang, X.; Hakim, L. F.; Zhan, G. D.; McCormick, J. A.; George, S. M.; Weimer, A. W.; Spencer, J. A.; Buechler, K. J.; Blackson, J.; Wood, C. J.; Dorgan, J. R. Novel Processing to Produce Polymer/Ceramic Nanocomposites by Atomic Layer Deposition. *J. Am. Ceram. Soc.* **2007**, *90*, 57−63.

(16) Thommes, M.; Kaneko, K.; Neimark, A. V.; Olivier, J. P.; Rodriguez-Reinoso, F.; Rouquerol, J.; Sing, K. S. W. Physisorption of gases, with special reference to the evaluation of surface area and pore size distribution (IUPAC Technical Report). *Pure Appl. Chem.* **2015**, *87*, 1051−1069.

(17) Sing, K. S. W. Reporting Physisorption Data for Gas/Solid Systems with Special Reference to the Determination of Surface Area and Porosity (Provisional). *Pure Appl. Chem.* **1982**, *54*, 2201−2218.

(18) de Zárate, D. O.; Gómez-Moratalla, A.; Guillem, C.; Beltrán, A.; Latorre, J.; Beltrán, D.; Amorós, P. High-Zirconium-Content Nano−Sized Bimodal Mesoporous Silicas. *Eur. J. Inorg. Chem.* **2006**, *2006*, 2572−2581.

(19) Babaie, F.; Mousavi, S. H.; Alizadeh, A. m.; Hazrati, N. Carbon Dioxide Capture by Modified UVM-7 Adsorbent. *J. Chem. Pet. Eng.* **2014**, *48*, 91−102.

(20) Park, E. J.; Lee, J. H.; Kim, K. D.; Kim, D. H.; Jeong, M. G.; Kim, Y. D. Toluene Oxidation Catalyzed by NiO/SiO_2 and NiO/TiO_2/SiO_2: Towards Development of Humidity-Resistant Catalysts. *Catal. Today* **2016**, *260*, 100−106.

(21) Hengne, A. M.; Samal, A. K.; Enakonda, L. R.; Harb, M.; Gevers, L. E.; Anjum, D. H.; Hedhili, M. N.; Saih, Y.; Huang, K. W.; Basset, J. M. Ni-Sn-Supported ZrO_2 Catalysts Modified by Indium for Selective CO_2 Hydrogenation to Methanol. *ACS Omega* **2018**, *3*, 3688−3701.

(22) Biesinger, M. C.; Payne, B. P.; Lau, L. W. M.; Gerson, A.; Smart, R. S. C. X-Ray Photoelectron Spectroscopic Chemical State Quantification of Mixed Nickel Metal, Oxide and Hydroxide Systems. *Surf. Interface Anal.* **2009**, *41*, 324−332.

(23) Sompech, S.; Dasri, T.; Thaomola, S. Preparation and Characterization of Amorphous Silica and Calcium Oxide from Agricultural Wastes. *Orient. J. Chem.* **2016**, *32*, 1923−1928.

(24) Munasir; Triwikantoro; Zainuri, M.; Darminto. Synthesis of SiO_2 Nanopowders Containing Quartz and Cristobalite Phases from Silica Sands. *Mater. Sci.-Pol.* **2015**, *33*, 47−55.

(25) Miguel, C. V.; Trujillano, R.; Rives, V.; Vicente, M. A.; Ferreira, A. F. P.; Rodrigues, A. E.; Mendes, A.; Madeira, L. M. High Temperature CO_2 Sorption with Gallium-Substituted and Promoted Hydrotalcites. *Sep. Purif. Technol.* **2014**, *127*, 202−211.

(26) Haskouri, J. E.; Dallali, L.; Fernández, L.; Garro, N.; Jaziri, S.; Latorre, J.; Guillem, C.; Beltrán, A.; Beltrán, D.; Amorós, P. ZnO Nanoparticles Embedded in UVM-7-like Mesoporous Silica Materials: Synthesis and Characterization. *Phys. E* **2009**, *42*, 25−31.

(27) Vikrant, K.; Deng, Y. X.; Kim, K. H.; Younis, S. A.; Boukhvalov, D. W.; Ahn, W. S.; Deep, A. Application of Zr-Cluster-Based MOFs for the Adsorptive Removal of Aliphatic Aldehydes (C1 to C5) from an Industrial Solvent. *ACS Appl. Mater. Interfaces* **2019**, *11*, 44270−44281.

(28) Wang, Y.; Yang, D.; Li, S.; Chen, M.; Guo, L.; Zhou, J. Ru/Hierarchical HZSM-5 Zeolite as Ef Fi Cient Bi-Functional Adsorbent/Catalyst for Bulky Aromatic VOCs Elimination. *Microporous Mesoporous Mater.* **2018**, *258*, 17−25.

(29) Urbutis, A.; Kitrys, S. Dual Function Adsorbent-Catalyst CuO-CeO_2/NaX for Temperature Swing Oxidation of Benzene, Toluene and Xylene. *Open Chem.* **2014**, *12*, 492−501.

https://doi.org/10.1021/acs.energyfuels.2c01013
Energy Fuels XXXX, XXX, XXX−XXX